IOP Publishing Journal of Physics: Condensed Matter
J. Phys.: Condens. Matter **32** (2020) 275103 (11pp) https://doi.org/10.1088/1361-648X/ab7e5c

Phase behavior of a two-dimensional core-softened system: new physical insights

Luis A Padilla[1] **and Abelardo Ramírez-Hernández**[1,2]

[1] Department of Biomedical Engineering and Chemical Engineering, The University of Texas at San Antonio, San Antonio, TX 78249, United States of America
[2] Department of Physics and Astronomy, The University of Texas at San Antonio, San Antonio, TX 78249, United States of America

E-mail: luisadrian.padillasalas@utsa.edu and abelardo.ramirez-hernandez@utsa.edu

Received 15 October 2019, revised 20 February 2020
Accepted for publication 10 March 2020
Published 9 April 2020

Abstract

In this work, we report results of extensive computer simulations regarding the phase behavior of a core-softened system. By using structural and thermodynamic descriptors, as well as self-diffusion coefficients, we provide a comprehensive view of the rich phase behavior displayed by the particular instance of the model studied in here. Our calculations agree with previously published results focused on a smaller region in the temperature–density parameter space (Dudalov *et al* 2014 *Soft Matter* **10** 4966). In this work, we explore a broader region in this parameter space, and uncover interesting fluid phases with low-symmetry local order, that were not reported by previous works. Solid phases were also found, and have been previously characterized in detail by (Kryuchkov *et al* 2018 *Soft Matter* **14** 2152). Our results support previously reported findings, and provide new physical insights regarding the emergence of order as disordered phases transform into solids by providing radial distribution function maps and specific heat data. Our results are summarized in terms of a phase diagram.

Keywords: mesophases, quasicrystals, self-assembly

(Some figures may appear in colour only in the online journal)

1. Introduction

Colloidal nanocrystals are composed by a hard core material surrounded by a soft, organic component grafted onto the core's surface. The immense number of different organic ligands that can be used to decorate the core material makes it possible to tailor the effective interactions between these colloids. In fact, experiments have demonstrated that these materials can self-assemble into a rich variety of simple and complex lattices [1–4]. Therefore, providing a platform to design materials with exquisite functionalities. On the theoretical side, these materials are so complex that a first-principles approach to predict the mesoscopic ordering, from the chemical details, is utterly hopeless. However, based on effective interactions and a few parameters, coarse-grained descriptions can provide useful knowledge toward the understanding of the collective processes leading to the self-assembly of these materials [5–32].

Indeed, simple coarse-grained models have been used in the last decades to study mesophase formation and other collective phenomena [33–36]. A particularly interesting problem is that of two-dimensional (2D) melting. In three-dimensions the melting of solids is mostly a first-order phase transition, however the melting transition for parallel hard cubes in three-dimensions has been shown to be a second-order transition [37]. For two-dimensions, different scenarios have been proposed for melting. The most widely accepted scenario, known as the Berezinskii–Kosterlitz–Thouless–Halperin–Nelson–Young (BKTHNY) theory, proposes two continuous transitions between solid and liquid phases, with an intermediate thermodynamic state called hexatic phase [38–42]. On the other

hand, another scenario introduced by Bernard and Krauth (BK) proposes a continuous transition between solid and hexatic phases, and a first-order transition between hexatic and liquid phases [43–46]. Experimental evidence suggests that the BK scenario describes the melting process [47]. To explore this phenomenon, the most commonly used models are the hard disk (HD) and hard core soft shoulder (HCSS) potentials.

In recent years, a smoothed version of HCSS model has also been studied, and it is used in this work. The most important point to highlight is that this model captures the salient features of colloidal nanocrystals: a rigid core and a soft shell composed of the grafted organic ligands. Thus, it is a good candidate to explore the self-assembly behavior of these materials. Previous work using an instance of this model have focused in the low temperature–high density regime, and have reported the formation of simple and complex lattices [27]. However, it is expected that at intermediate densities other mesophases could appear, and the fluid phase would also display interesting local correlations that are not present in the hard disk model [16, 17]. This work explores the phase behavior of this core-softened model, described in detail below, in a broader region of the temperature–density parameter space. We use molecular dynamics simulations to study the statistical behavior of this model. To obtain a complete thermodynamic characterization, pressure, internal energy, compressibility factor and specific heat were computed. Structural information is obtained by calculating the radial distribution function, orientational order parameters, and structure factor. To complete our study, we also report the self-diffusion coefficient obtained for all conditions explored in this work.

2. Model and methods

The repulsive shoulder potential studied in this work is defined as [26]:

$$u(r)/\epsilon = \left(\frac{\sigma}{r}\right)^{14} + \frac{1}{2}\left[1 - \tanh\left(k(r-\sigma_1)\right)\right], \qquad (1)$$

where r is the distance between two interacting sites, ϵ is the height of the repulsive shoulder, and σ can be considered as the hard core diameter, whereas σ_1 is the characteristic length scale of the shoulder. The constant k accounts for the steepness of the repulsive shoulder (see figure 1). In this work, we set $\sigma_1 = 1.35\sigma$, $k\sigma = 10.0$, and we use σ and ϵ as length and energy units, respectively.

The exploration of thermodynamic phases was performed by molecular dynamics simulations in the *NVT* ensemble with a Nosé–Hoover thermostat [48, 49]. All calculations were performed using HOOMD-blue [50, 51]. We consider square simulation boxes with periodic boundary conditions in all directions. The systems are composed by $N = 2^{15}$ particles at reduced densities $\rho^* \equiv N\sigma^2/A$, and reduced temperatures $T^* \equiv k_B T/\epsilon$. We explored the parameter space (ρ^*, T^*), with $\rho^* \in [0.1, 1.0]$ and $T^* \in \{0.8, 0.6, 0.5, 0.4, 0.3, 0.25, 0.22, 0.2, 0.18, 0.16, 0.14, 0.12, 0.1\}$. The density was varied in steps of $\delta\rho^* = 0.05$, unless otherwise noted. To avoid quenching effects at the lower temperatures, an annealing procedure was used: systems were prepared at a disordered state at highest temperature first, and then the final configuration is used as initial configuration for the next lower temperature, and so on. In every simulation, the system is equilibrated using 3×10^7 time steps at the corresponding temperature, then properties are sampled during the next 7×10^7 time steps. Post-processing of data is performed by using ten sub-blocks of the whole trajectory. The reduced timestep was set at $\delta t^* = \delta t\sqrt{\epsilon/m\sigma^2} = 0.001$, and the thermostat coupling constant to $\tau = \sqrt{Q/gk_BT} = 1.0$, where Q is the Nosé mass, g is the number of degrees of freedom, k_B is the Boltzmann constant, and T is the temperature. It should be highlighted that particle-based simulations are susceptible to display systematic errors when studying the phase behavior, due to fact that systems can get trapped into local free energy minima. Thus, efforts must be done to minimize such effects. In this work, the use of an annealing procedure helps in this regard.

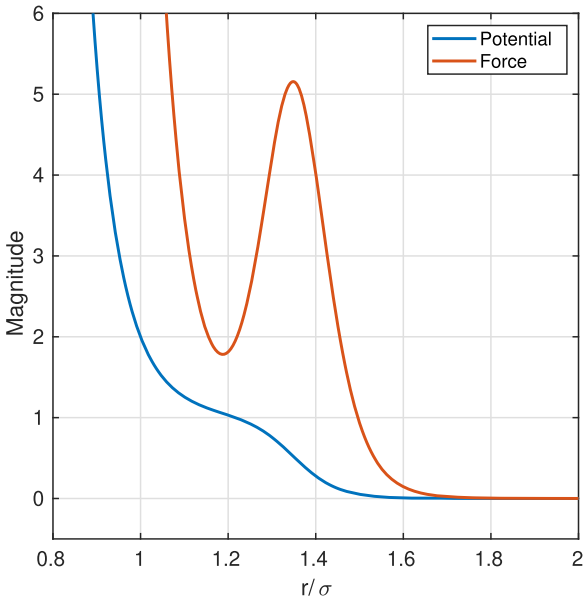

Figure 1. Soft repulsive shoulder potential (blue line) and associated force (red line) with parameters $\sigma_1 = 1.35\sigma$, $k\sigma = 10$. See text and equation 1 for details.

The thermodynamic behavior of the system is characterized by using the reduced internal energy $U^* \equiv U/N\epsilon$, reduced pressure $P^* \equiv P\sigma^2/\epsilon$, compressibility factor $Z \equiv P^*/(\rho^* T^*)$, and reduced specific heat $c_v^* \equiv C_v^*/N = C_v\epsilon^2/k_B N$; where the heat capacity, C_v, is defined by:

$$C_v = \frac{\langle U^2\rangle - \langle U\rangle^2}{k_B T^2}. \qquad (2)$$

To characterize the symmetry of the equilibrated structures, we use the bond orientational order (BOO) parameter, and the structure factor (SF). The global bond orientational order parameter is computed as [33]:

$$\chi_m = \left\langle \left| \frac{1}{N_B} \sum_j^{N_B} \exp(im\theta_j) \right|^2 \right\rangle, \qquad (3)$$

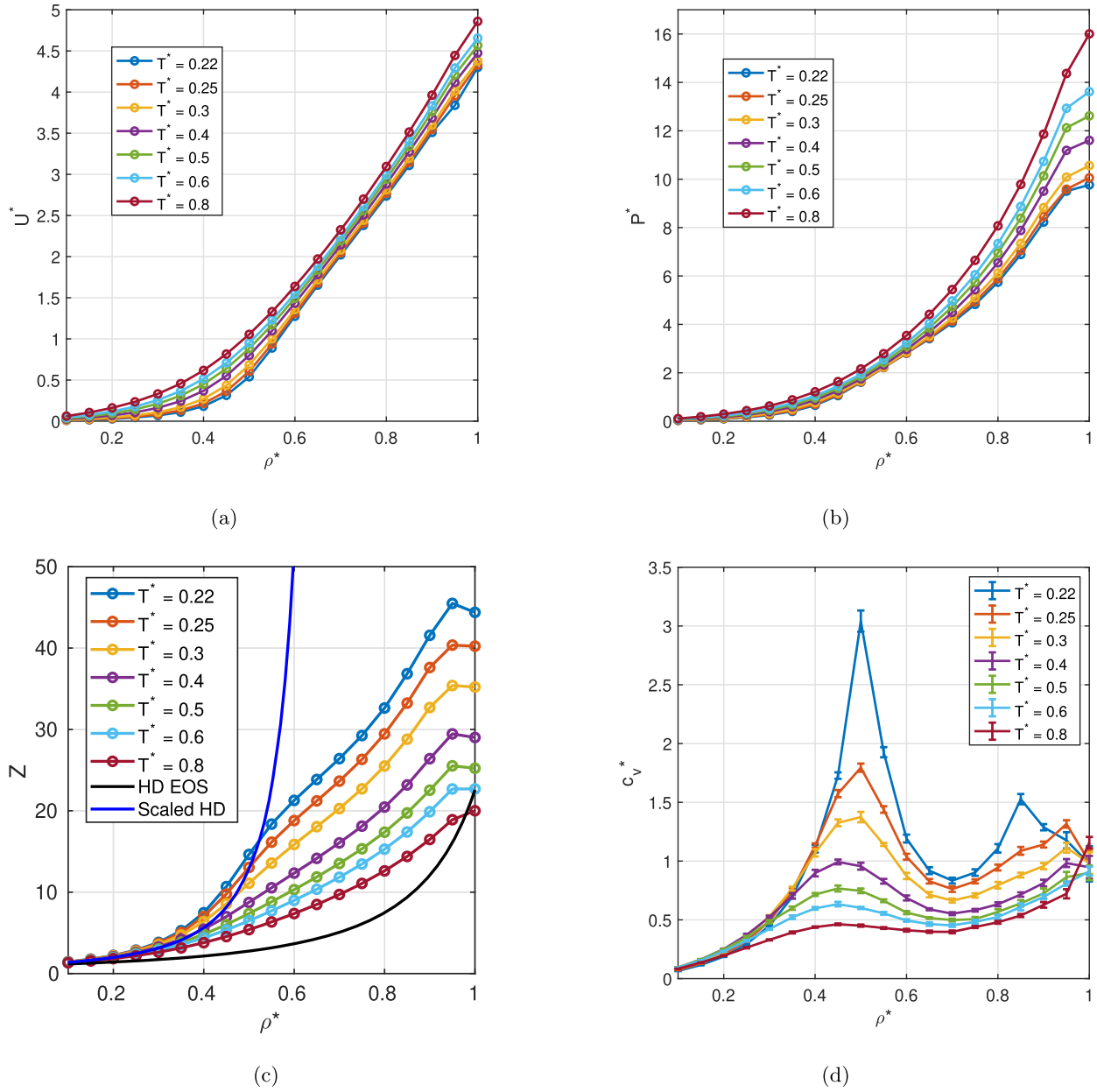

Figure 2. Thermodynamic descriptors for different temperatures in the interval $0.8 \geqslant T^* \geqslant 0.22$: (a) internal energy U^*, (b) pressure P^*, (c) compressibility factor Z, as functions of density ρ^*. The continuous black line in (c) is the EOS for hard disks proposed by Solana *et al* [54], and the continuous blue line is the same EOS but with effective diameter $\sigma_{\text{eff}} = 1.35$. The error bars in (a)–(c) are smaller than the symbols. (d) Specific heat c_v^* vs density ρ^*. The error bars are included for reference. Note the change of curvature of the compressibility factor, Z, in the same region where the specific heat displays a maximum at intermediate densities.

where m is an integer characterizing the symmetry, θ_j is the angle formed between a fixed axis and the bond connecting the jth pair of particles separated by no more than a distance λ; N_{B} is the number of neighbor bonds, and the brackets indicate ensemble average. As described below, at low densities and temperatures, the shoulder length scale dominates the separation between particles. At high densities, the hard core length scale dictates the separation. However, at intermediate density values, there is an interplay between these two length scales. Thus, the value of λ is determined as the first minimum after the global maximum of the radial distribution function, at a given temperature and density. Note that a local BOO parameter, $\chi_{m,k}$, can be obtained using the same expression, but N_{B} will now be the number of neighbor bonds of the kth particle. By taking an average of all local BOO, it is possible to obtain an insight about the local symmetry of the small domains formed by an arbitrary particle and its close neighbors.

The structure factor is given by [52]:

$$S(\vec{k}) = \frac{1}{N}\sum_{j}^{N} \exp(i\vec{k}\cdot\vec{r}_j), \tag{4}$$

where $\vec{k}$ is a wave vector, and $\vec{r}_j$ is the vector position of the jth particle. We also computed the radial distribution function

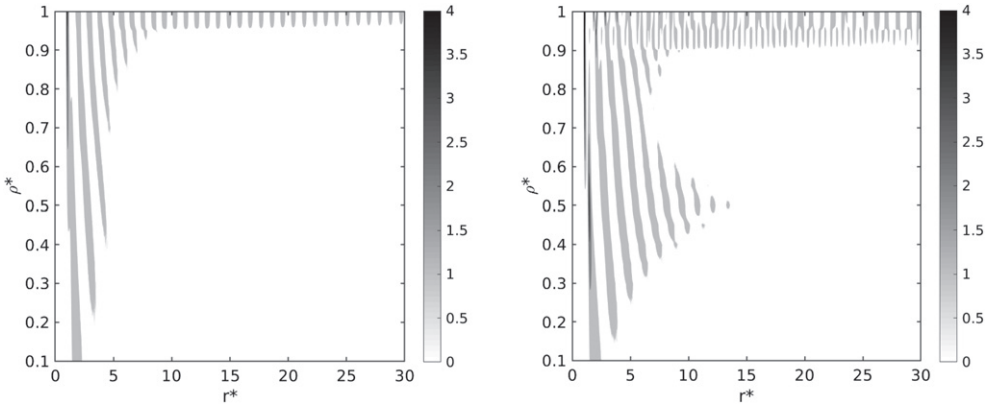

(a) $T^* = 0.80$ (b) $T^* = 0.22$

Figure 3. Density maps of the radial correlation function $h(r^*) = g(r^*) - 1$ on the (r^*, ρ^*) plane at the indicated temperature. Only values $h(r^*) \geqslant 0$ are plotted. In the high temperature case, (a), the particle–particle correlation builds-up as the density increases and long-range order appears at the highest density. In the low temperature case, (b), long-range order appears at lower densities. For $0.96 > \rho^* > 0.9$, a solid phase with a 12-fold symmetry appears, but at higher densities an hexagonal solid becomes stable. Interestingly, particle–particle correlations increase in range at intermediate densities, in the same region where the specific heat displays a maximum (see figure 2(d)).

(RDF) as [53]:

$$g(r) = \frac{A}{N^2}\sum_{i}^{N}\sum_{j\neq i}^{N}\delta(r - r_{ij}), \tag{5}$$

where A is the area of the simulation box, and r_{ij} is the distance between the ith and jth particles.

Finally, the mean squared displacement (MSD):

$$\left\langle(\vec{r}(t) - \vec{r}_0)^2\right\rangle = \frac{1}{N}\sum_{i=1}^{N}(\vec{r}_i(t) - \vec{r}_i(0))^2, \tag{6}$$

and the associated self-diffusion coefficient D were also computed. To obtain D, a linear fit was performed over the MSD vs t curves at long times. Then, we used the following relationship

$$\left\langle(\vec{r}(t) - \vec{r}_0)^2\right\rangle = 2dDt, \tag{7}$$

where d is the dimensionality of the system.

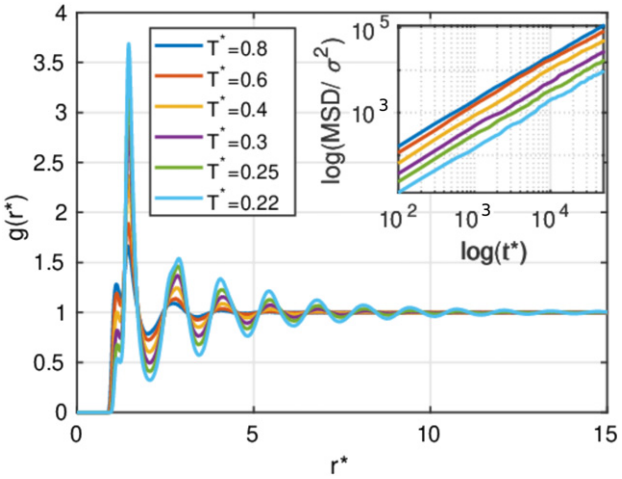

Figure 4. Radial distribution function at density $\rho^* = 0.5$ for different temperatures T^*. Inset: MSD for all temperatures on the main plot. Note that the range of correlation increases as temperature decreases, and the system is still in a fluid phase.

3. Results

3.1. High temperature regime

We start our analysis by presenting the isotherms for internal energy, pressure, compressibility factor, and specific heat as functions of density (figure 2) in the high temperature regime, $0.8 \geqslant T^* \geqslant 0.22$. In the case of internal energies, U^*, it is found that the different isotherms display a similar behavior, and there is no evidence of discontinuities nor abrupt changes in the shape of the isotherms (figure 2(a)). The behavior of the pressure as the density is varied is similar for the different temperatures (figure 2(b)). However, as the density approaches $\rho^* = 1.0$, there is a change in the curvature of the P^* vs ρ^* curve, which we associate with the transition to a solid with a triangular lattice. This agrees with the findings in reference [27] at low temperatures.

On the other hand, the compressibility factor, Z, displays an interesting behavior (see figure 2(c)). First, note that, as expected, at low densities (up to $\rho^* = 0.3$), the behavior of the system is almost athermal, as in the case of a hard disks system. For comparison, we have also plotted the equation of state (EOS) for hard disks proposed by Solana *et al* [54]. Small deviations (at low densities) from the HD EOS arise because of the soft shoulder, which renormalizes the effective particle diameter. The most interesting behavior occurs at the interval $0.4 \leqslant \rho^* \leqslant 0.6$, where thermal effects become more evident. In this zone, the compressibility factor increases at a much faster rate as the density increases. This is, in fact, reflected as a change in the concavity of the Z vs ρ^* curve (see figure 2(c)). This behavior suggests a drastic change on the particle configurations, and could indicate the presence of a second or higher

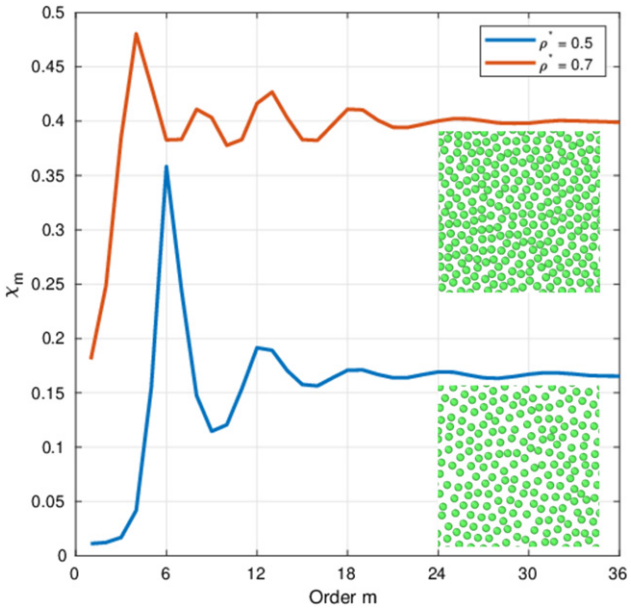

Figure 5. Local bond orientational order as a function of the order m at $T^* = 0.25$. A snapshot of particle configuration at the indicated density is displayed below the corresponding curves. The global BOO vanishes for all m, however these liquids have a local orientational order.

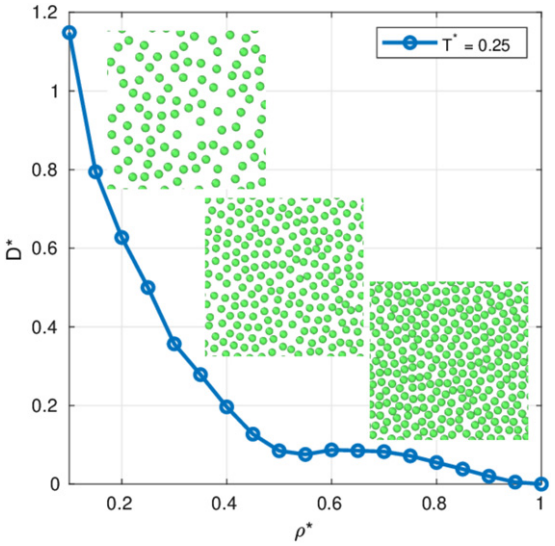

Figure 7. Self-diffusion coefficient, D^*, at different densities ρ^*, at temperature $T^* = 0.25$. Insets show representative particle configurations for $\rho^* = 0.3, 0.5, 0.7$, from top to bottom, respectively. Anomalous behavior of D^* occurs at intermediate densities where the thermodynamic descriptors display features of structural changes.

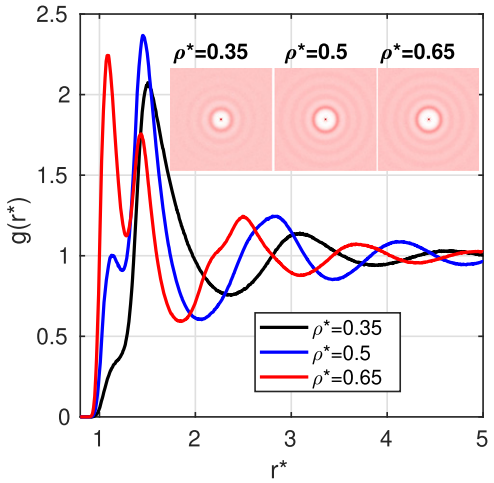

Figure 6. Radial distribution function at different densities ρ^*, at temperature $T^* = 0.4$. Insets show the associated structure factors. Note that the system can be seen as composed by particles of sizes σ and σ_1. The concentration of one component changes as the density and temperature are varied.

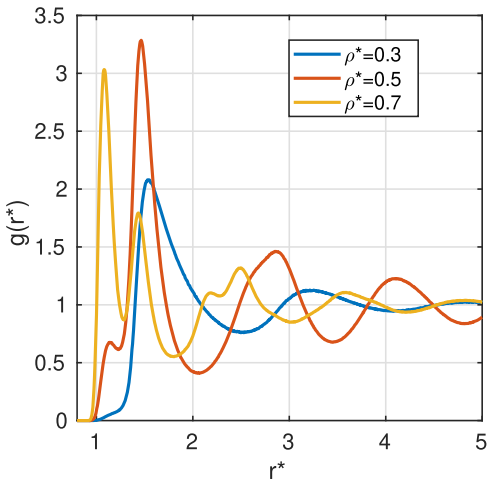

Figure 8. Radial distribution functions associated to those fluid states at the minimum and maximum of the D vs ρ curve shown in figure 7 ($T^* = 0.25$). As can be seen, at the minimum of D (at $\rho = 0.5$), the local structural order is higher than that presented at the maximum of D (at $\rho = 0.7$), see text for details.

order phase transition. For higher densities, up to $\rho^* = 0.85$, the changes in Z are not as strong, thus, phase transitions are not expected in this thermodynamic region. Finally, at the high density regime, the compressibility has an abrupt change, as the one displayed by the pressure, which is an evidence of a first order phase transition, from the disordered phase to the hexagonal phase.

The intriguing behavior of Z at intermediate densities motivated us to compute the specific heat for the same temperature range. As can be seen in figure 2(d), a small hump arises around $\rho^* = 0.45$ already for $T^* = 0.8$. As the temperature decreases, the hump increases its size drastically, and the local maximum shifts to slightly higher densities. Two things can be inferred by this behavior: (a) there are significant structural changes in the fluid phase that become more noticeable at lower temperatures (we will discuss these changes below); (b) the behavior of c_v^* as the temperature decreases (along with the fact that internal energy and pressure do not display discontinuities), suggests that a critical point exists in this region on the parameter space. Also, note that a second peak starts to develop at densities around $\rho^* = 0.85$ at low temperatures, which corresponds to the region studied by Kryuchkov *et al* [27]. In this part of the phase diagram they found square and

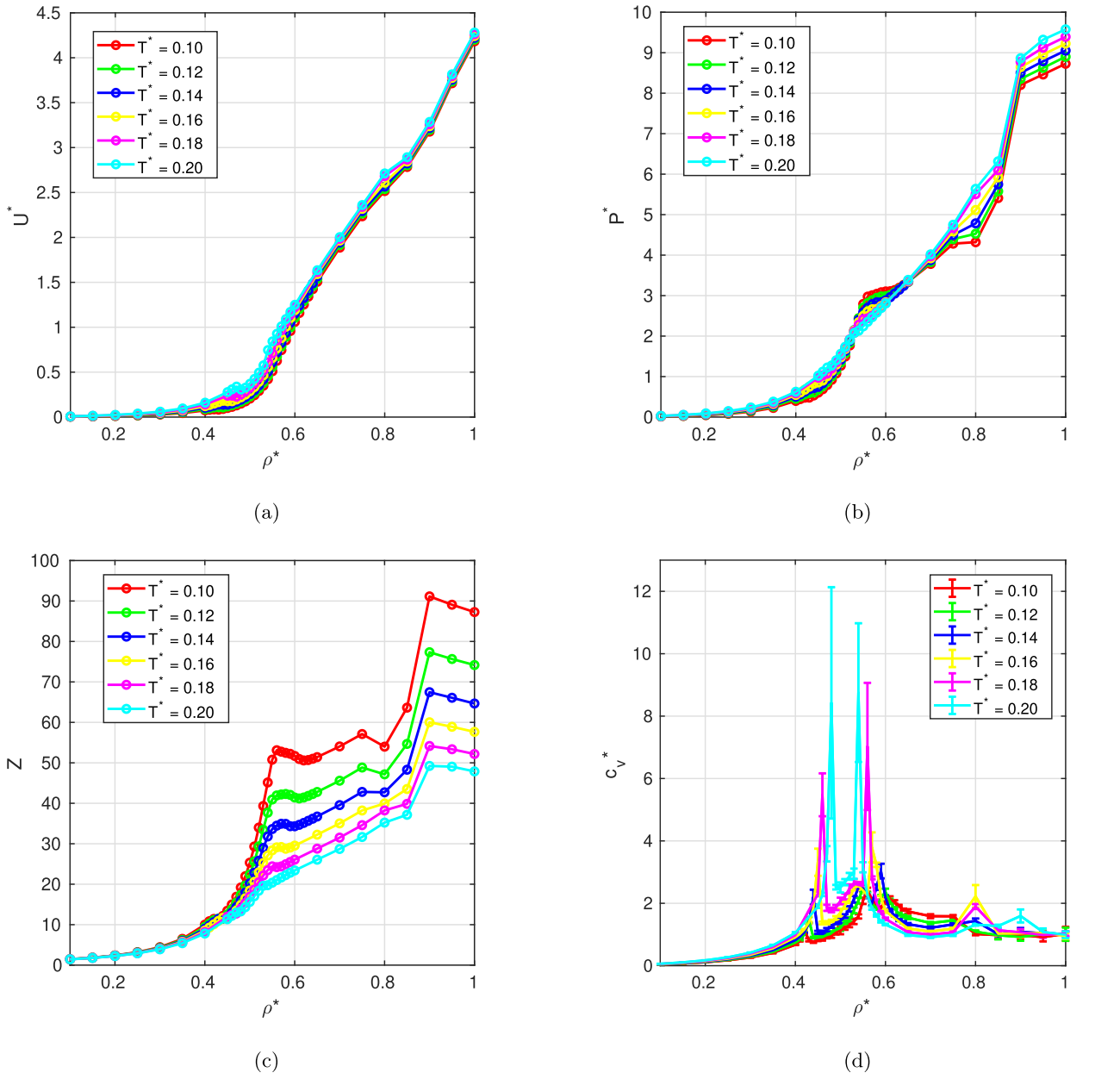

Figure 9. Thermodynamic descriptors for different temperatures in the interval $0.2 \geqslant T^* \geqslant 0.1$: (a) internal energy U^*, (b) pressure P^*, (c) compressibility factor Z, as functions of density ρ^*. The error bars in (a)–(c) are smaller than the symbols. (d) Specific heat c_v^* vs density ρ^*. The error bars are included for reference. The behavior of the specific heat at intermediate densities suggest the existence of re-entrant phase transitions. At higher densities, the behavior of the pressure indicates a first-order phase transition to solid phases, as shown below.

hexagonal solids, and 12-fold quasicrystals. As we report below, our calculations agree with their results (see figures 13(c) and (d)).

The above results suggest that the liquids at intermediate densities have interesting properties. Thus, we use structural descriptors to characterize these fluid phases. Figure 3 displays density maps of the radial distribution function (RDF) on the (r^*, ρ^*) plane. We present only the results for temperatures $T^* = 0.8$ and 0.22. For the highest temperature, $T^* = 0.8$, the associated RDF map shows how local order starts to building-up, and eventually, long-range order appears for the highest density (see figure 3(a)). BOO parameter and structure factor indicate that the formed structure at that high density is a solid phase with hexagonal symmetry (data not shown). This phenomenology agrees with features observed on the thermodynamic descriptors presented above. The discontinuity in the pressure that appears at high density correlates with the emergence of a dominant symmetry and the corresponding long-range correlations. As the temperature is decreased to $T^* = 0.22$, the RDF map displays more interesting features (figure 3(b)). First, at high densities (above $\rho^* \sim 0.9$) it is possible to see the emergence of long-range correlations, and the RDF uncover two different particle arrangements. Indeed, BOO and structure factor indicate that the fluid transforms into a solid phase with a 12-fold symmetry (data not shown). This structure corresponds to the dodecagonal

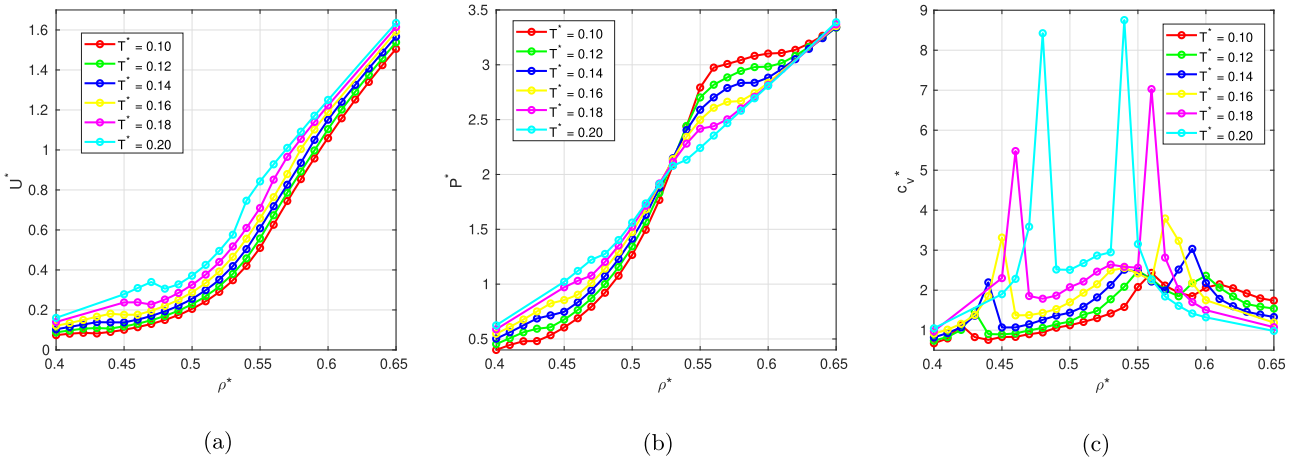

Figure 10. Thermodynamic descriptors for different temperatures in the interval $0.2 \geqslant T^* \geqslant 0.1$ at intermediate densities $0.65 \geqslant \rho^* \geqslant 0.4$: (a) internal energy U^*, (b) pressure P^*, and (c) specific heat c_v^* as functions of density ρ^*. By enlarging this zone, it is clear that the stability region of the low-density solid phase increases as temperature decreases. Also, note the asymmetry on the behavior of c_v^* at low and high density: for $T^* < 0.16$, the peak of c_v^* on the right splits into two.

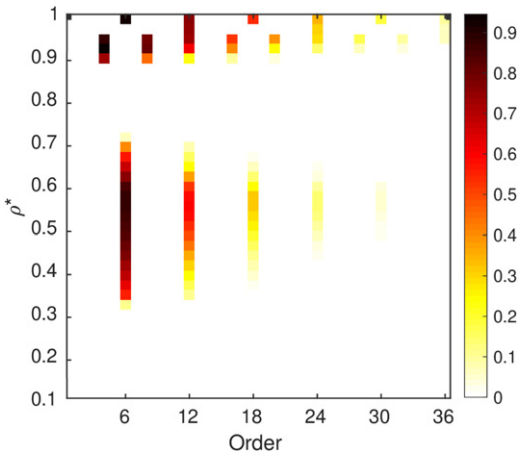

Figure 11. Color map of global bond orientational order, χ_m, on the (m, ρ^*) plane at $T^* = 0.12$. The color bar show the correspondence between color and the value of the bond orientational order. This plot clearly shows that re-entrant transitions occurs at intermediate densities, and the existence of a low density solid phase with six-fold symmetry.

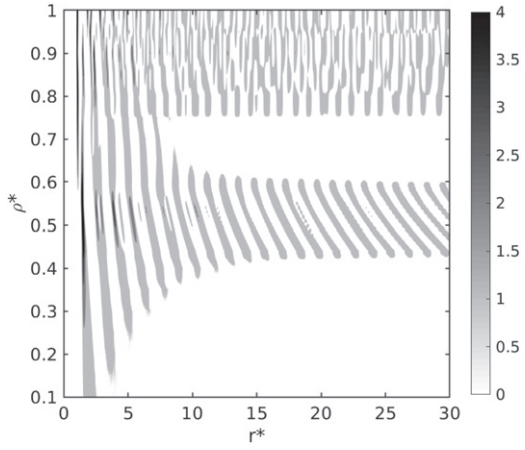

Figure 12. Density map of the radial correlation function $h(r^*) = g(r^*) - 1$ on the (r^*, ρ^*) plane at temperature $T^* = 0.12$. We plot only values $h(r^*) \geqslant 0$. Note that long-range correlations appear at intermediate densities, the region where the global BOO indicates a phase with a six-fold symmetry.

quasicrystal found by Kryuchkov *et al* [27]. For densities above $\rho^* \sim 0.96$ the quasicrystal losses stability, and a solid with hexagonal order dominates. Interestingly, for the densities around $\rho^* = 0.5$, the RDF map shows that the correlation among particles has a range larger than that displayed by the isotropic states in the neighboring densities. This coincides with the bump observed in the specific heat curves on the same density region (see figure 2(d)). Thus, thermodynamic and structural descriptors display a signature that indicates a significant change in the local order, even though there is not a collective symmetry-breaking process involved at this temperature. These are still (globally) isotropic fluid states, and the local order arises as a delicate balance between energy and entropy. At intermediate and low temperatures, some particles do not have enough energy to overcome the barrier associated to the shoulder. Thus, the population of nearest neighbors contains two contributions: one coming from those particles separated by $\sim \sigma$, and the other, composed by particles separated by a distance $\sim \sigma_1$. The relative weight depends on both the density and temperature. For example, figure 4 displays the radial distribution function at $\rho^* = 0.5$ for different temperatures. As can be seen, by decreasing temperature, the number of particles able to cross the soft shoulder decreases. At this density, there is still room to accommodate particles apart by the soft length scale, so, the system favors a local order where particles will be placed close to a distance $\sim \sigma_1$ from each other, in average. Indeed, the local BOO spectrum (figure 5) confirms that, for this density ($\rho^* = 0.5$), there is a preference for local order with a six-fold symmetry. However, the global BOO indicates the lack of a dominant global symmetry. The MSD curves shown at the insets of figure 4 demonstrate that the systems display normal diffusion at long times, as expected for fluid phases. Thus, these are locally ordered liquids.

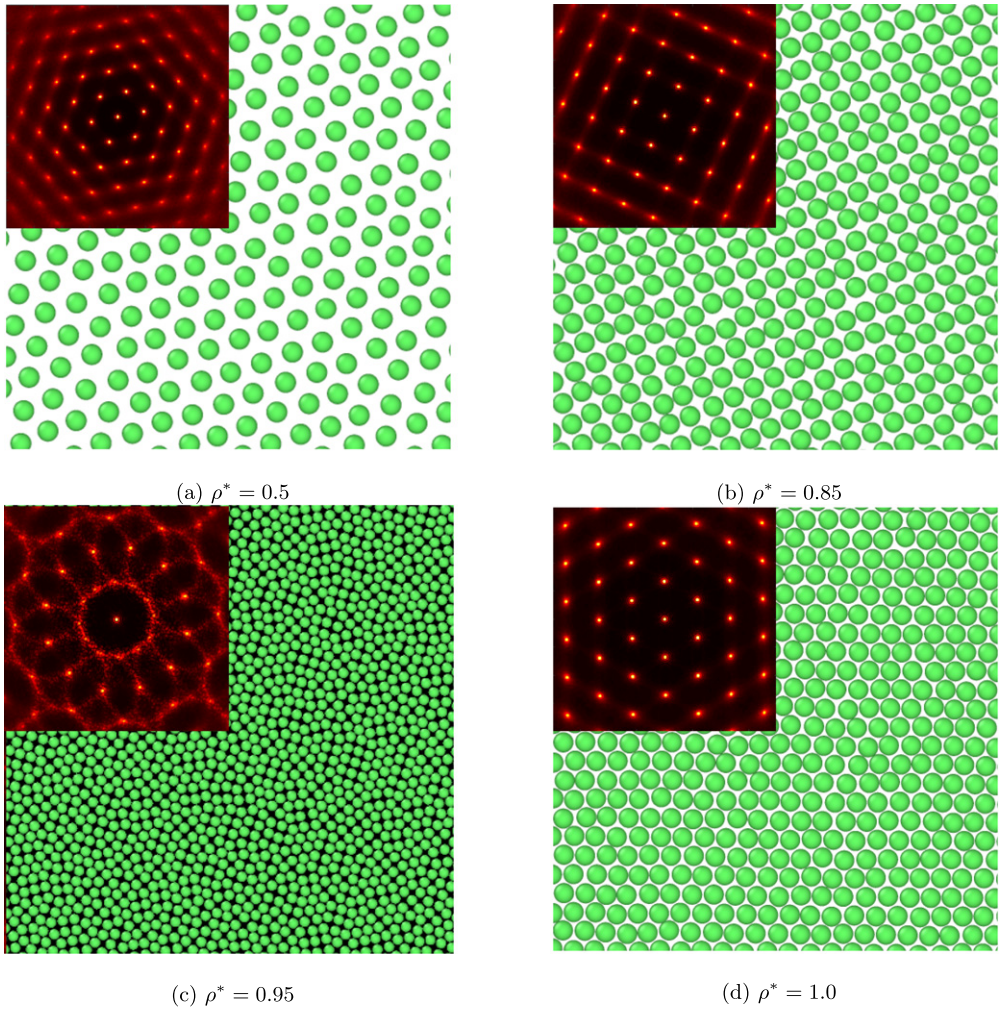

Figure 13. Snapshots of a small section of the simulation box for systems at temperature $T^* = 0.12$ and different densities. The associated structure factors are shown as insets: (a) six-fold symmetry, (b) four-fold symmetry, (c) 12-fold symmetry, and (d) six-fold symmetry. Note that, even though there are two hexagonal solid phases, the scattering pattern is different. The lattice constant of the low-density phase is larger than the corresponding lattice constant at the highest density (see text for details). Note that the scale in the snapshot (c) is different, to make evident the quasicrystalline organization. All configuration snapshots were created by using Ovito [60].

The distribution of neighbors located at σ and σ_1 is also affected by the density. As shown in figure 6, by increasing density, particles are forced to be closer, and more particles are located around a distance σ from each other. Thus, at these intermediate densities and temperatures the system can be considered as a fluid mixture of particles of effective diameters σ and σ_1. The energetic balance dictates the local order that these particles will adopt. The red curve in figure 5 shows that, for $\rho^* = 0.7$, there is a slight preference for a local order with a four-fold symmetry. This local orientational order has also effects on the dynamical behavior of these fluids. We have computed the self-diffusion coefficient, $D^* = D/\sqrt{\sigma^2\epsilon/m}$, for temperature $T^* = 0.25$. As can be seen in figure 7, D^* displays a non-linear behavior at intermediate densities, and that is a consequence of the local order that arose in these fluids at this region of the parameter space (see insets in figure 7). In all cases the global BOO vanishes, but there is still local orientational order. Besides of the local orientational order, local structural order is present. Figure 8 displays the radial distribution function, $g(r)$, associated to the fluid states at the minimum and maximum of the D vs ρ curve. As can be seen, at the minimum of D (at $\rho = 0.5$), the local structural order is higher than that presented at the maximum of D (at $\rho = 0.7$). This anomalous behavior arises because once the density is high enough such that particles have already overcome the soft barrier, and all coronas are overlapped, the effective repulsion is smaller. Thus, given place to a less structural order. It should be also noted that core-softened potentials display several anomalous behavior [55–57], in particular, a density anomaly can be present. This anomaly can be seen by analyzing the density versus temperature isobars when performing NPT simulations [58].

3.2. Low temperature regime

Next, we study the low temperature regime $0.2 \geqslant T^* \geqslant 0.1$. The results for the same thermodynamic descriptors used above are presented in figure 9. To get more details about the behavior at intermediate densities, we have used a smaller $\delta\rho^*$ in that region. As can already be seen in the behavior of

the internal energy (figure 9(a)), at these temperatures, there are at least three different phase transitions. Two of them at intermediate densities ($0.4 \leqslant \rho^* \leqslant 0.6$), and one around $\rho^* = 0.8$. The latter can be ascribed to the liquid-square solid transition, already found in reference [27]. Pressure and compressibility curves also display signatures of phase transitions (see figures 9(b) and (c)). Whereas the transition at high density ($\rho^* \sim 0.8$) display a strong first-order character (note the big jump on the values of pressure or compressibility), it is hard to infer the order of the transitions at intermediate densities. On one hand, U^*, P^*, and Z do not display any jumps or discontinuities at transition points, but just a change in the slope. Also, the specific heat displays a rapid increase in value as one approaches the transition points (see figure 9(d)), a feature of a second-order phase transition. On the other hand, as can be seen in figures 10(a) and (b), U^* and P^* seem to display weak Mayer–Wood loops which can be associated to first-order phase transitions [59]. Thus, we can not establish the exact nature of these transitions with the current data. To address this interesting problem, it is required to perform analysis of system size effects, calculation of other correlation functions, etc. This study is left for a future work.

To elucidate the symmetry of the phases found at these low temperatures, the global BOO parameter spectrum can be used. For example, at the temperature, $T^* = 0.12$, it is possible to observe symmetry-breaking processes, where the values of χ_m are very small for most of the m values, and one of them, $m^\star$ (and its integer multiples), dominates the symmetry of the system. In fact, a square phase ($m^\star = 4$) becomes stable between $\rho^* \sim 0.75$ and $\rho^* \sim 0.95$, as clearly seen in the global BOO parameter density map (figure 11). The liquid–solid transition corresponds to the discontinuity observed in the pressure (see figure 9(b)). The RDF suggests that this is a solid phase with long-range correlations (see figure 12). At higher densities, both 12-fold quasicrystal and hexagonal solids are found (figure 11). Interestingly, the RDF map indicates that, at intermediate densities, a new phase with long-range correlations exists (figure 12). The stability boundaries correspond to the peaks on the specific heat displayed in figure 9(d), thus both structural descriptors suggest it to be a new thermodynamic phase. The global BOO parameter (figure 11), clearly identifies it as a phase with hexagonal symmetry, $m^\star = 6$. To complement our analysis we also computed the structure factor associated to each of the different solid phases identified on the BOO map. The corresponding structure factors are shown in figure 13. From these plots we corroborate that the symmetry of low density phase corresponds to an hexagonal solid, also, it can be seen that the structure factor is much more diffuse far from the center than the corresponding one for the hexagonal solid at high density, $\rho^* = 1.0$ (figure 13(d)). Although, the symmetry is the same, these are different solids: the average distance between particles in this structure ($\rho^* = 0.5$) is $d^* \sim 1.48$, whereas in the hexagonal solid at $\rho^* = 1.0$ has $d^* \sim 1.06$. Thus, the former solid arises because at low temperatures the particles do not have enough energy to overcome the energy barrier associated to the shoulder. So, they behave like solid disks with an effective radius that depends on the density and shoulder range. Both BOO and RDF density maps clearly show the existence of re-entrant isotropic–hexagonal–isotropic transitions at intermediate densities. Also, the specific heat indicates, as deduced from the location of the peaks in this function, that the region of stable hexagonal phase broadens as the temperature decreases (see figure 10(c)). We should note here that previous works, with similar models, have found evidence of a low-density solid [61, 62]. However, such calculations were focused on the very low temperature limit.

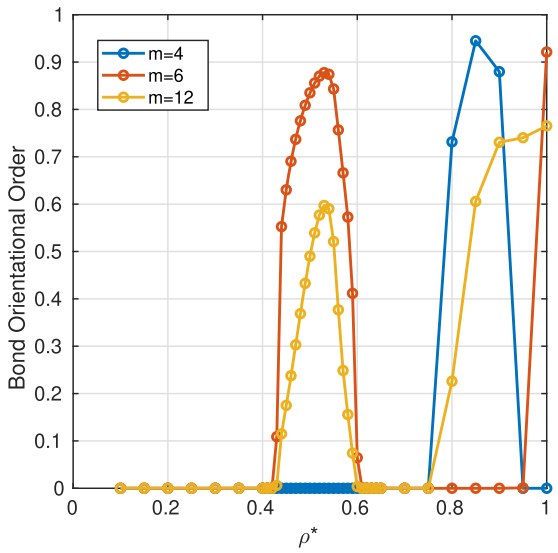

Figure 14. Global bond orientational order parameter, χ_m, as a function of the density for $m = 4, 6, 12$ at $T^* = 0.12$. The BOO associated to the low-density solid phase displays an asymmetric behavior as it reaches the stability boundaries.

Interestingly, there is an asymmetry on the behavior of c_v^* between the low- and high-density stability limits. (figure 10(c)). On the low-density side, the peak of c_v^* moves toward smaller densities as the temperature decreases, and the value of the peak decreases in magnitude. On the high-density side there is a peculiar behavior: at temperatures lower than 0.18, the peak of c_v^* splits into two peaks (or bumps) with smaller magnitude. This suggests the existence of another phase transition, possibly between the hexagonal solid and an hexatic phase. More work is required to elucidate the nature of this phase transition. The asymmetry is also reflected on the behavior of the relevant global BOO parameters. Figure 14 displays $\chi_4(\rho^*)$, $\chi_6(\rho^*)$, and $\chi_{12}(\rho^*)$ at $T^* = 0.12$. As can be seen in this figure, on the high-density side, the six-fold order parameter decays faster than in the other stability boundary. This interesting result warrant further studies.

We end the analysis by presenting a color map of the self-diffusion coefficient, D^*, computed for all systems studied in this work (figure 15). As expected, those regions on the parameter space where solid phases are found have a vanishing diffusion coefficient, both at high and intermediate densities. As described above, also note the peculiar behavior displayed at intermediate densities and temperatures: the self-diffusion coefficient seems to have a complicated non-linear behavior. This region corresponds to the isotropic liquids with high local order.

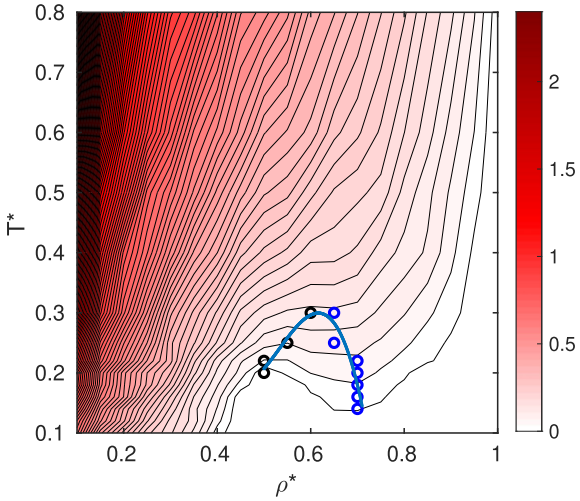

Figure 15. Color map of the self-diffusion coefficient, D^*, on the (ρ^*, T^*) plane, contour lines are also displayed. Note the strong non-linear behavior of D^* at intermediate densities where local order is stronger. As expected, D^* vanishes in those areas where solid phases appear. The plot also shows the temperature of maximum (blue) and minimum (black) diffusion coefficients (see figure 7).

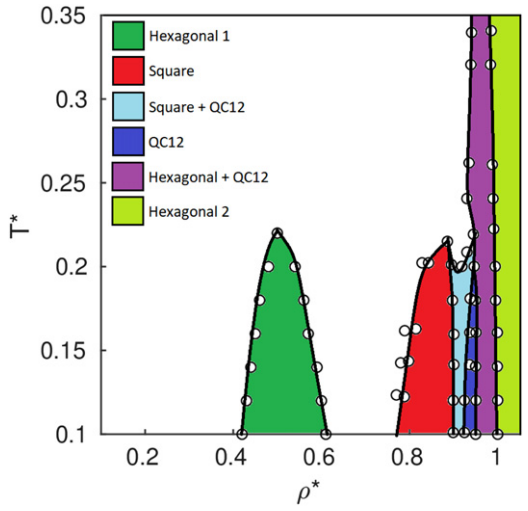

Figure 16. Phase diagram of the system studied in this work in the ρ–T plane. We have used data from reference [27] and results reported in this work. Low and high density hexagonal solids are indicated by hexagonal 1 and hexagonal 2. Square solids (square) and quasicrystal with 12-fold symmetry (QC12) are also found. We have also indicated coexistent regions. The broad white area consists of isotropic states.

All simulation results obtained in this work are summarized in terms of a phase diagram in figure 16. It should be noted the great similarity between the phase diagram associated to this model and that of a hard disk with a soft corona with a very similar interaction range [63]. In reference [63], Monte Carlo simulations were performed to study the stability of quasicrystals and other lattices, and found square solids and quasicrystalline states in small regions of the parameter space. The low-density hexagonal phase has a stability region around the same thermodynamic parameters in both models. However, the quasicrystal and square solid appear at higher densities in the discontinuous model, and they survive at higher temperatures compared to those present in the model used in this work (compare phase diagram in this work, figure 16, with figure 3 in reference [63]). Low-density hexagonal phases have also been found in other soft models. For example, reference [55, 56] reported the existence of hexagonal phases at intermediate densities, moreover, one of the models also displayed square solid phases.

4. Conclusions

We have performed extensive computer simulations of a two-dimensional core-softened model that displays a rich phase diagram (figure 16). Including simple and complex lattices at high densities and low temperatures, and more interestingly, a re-entrant isotropic–hexagonal–isotropic behavior at intermediate densities and low temperatures. We have also found a region dominated by fluids with a high local order, although, there is not a collective dominant symmetry. This anomalous structural behavior also affects the dynamical behavior as the associated diffusion coefficient displays a complicated non-linear dependence on temperature and density. The transition from isotropic and locally structureless fluids to these fluids with high local order can only be identified by second order thermodynamic properties (specific heat), which show strong variations in this region of the parameter space, such changes could suggest a high-order transition between these fluids.

As mentioned in the introduction, the model studied in this work is a good approximation to colloidal nanocrystals. Thus, it would be interesting to corroborate if the phases that we have found are realized experimentally.

Acknowledgments

A R-H acknowledges the start-up support of the Faculty Science and Technology Acquisition and Retention (STARs) Program from UT System. This work received computational support from UTSA's HPC cluster SHAMU, operated by University Technology Solutions. The authors are grateful for valuable computing resources provided by the Texas Advanced Computing Center (TACC) at The University of Texas at Austin (URL: http://www.tacc.utexas.edu).

ORCID iDs

Abelardo Ramírez-Hernández https://orcid.org/0000-0002-3569-5223

References

[1] Jishkariani D, Elbert K C, Wu Y, Lee J D, Hermes M, Wang D, van Blaaderen A and Murray C B 2019 *ACS Nano* **13** 5712–9
[2] Girard M, Wang S, Du J S, Das A, Huang Z, Dravid V P, Lee B, Mirkin C A and de la Cruz M O 2019 *Science* **364** 1174–8
[3] Boles M A, Engel M and Talapin D V 2016 *Chem. Rev.* **116** 11220–89

[4] Talapin D V, Lee J S, Kovalenko M V and Shevchenko E V 2010 *Chem. Rev.* **110** 389–458
[5] Kozak J J, Brzezinski J and Rice S A 2008 *J. Phys. Chem.* B. **112** 16059
[6] Moucka F and Nezbeda I 2005 *Phys. Rev. Lett.* **94** 040601
[7] Zhou S and Solana J R 2009 *J. Chem. Phys.* **131** 204503
[8] Kapfer S C and Krauth W 2015 *Phys. Rev. Lett.* **114** 035702
[9] Terao T 2013 *J. Chem. Phys.* **139** 134501
[10] Iacovella C R, Keys A S and Glotzer S C 2011 *Proc. Natl Acad. Sci.* **108** 20935
[11] Gribova N V, Fomin Y D, Frenkel D and Ryzhov V N 2009 *Phys. Rev.* E. **79** 051202
[12] Engel M, Damasceno P F, Phillips C L and Glotzer S C 2015 *Nat. Mater.* **14** 109–16
[13] Keys A S and Glotzer S C 2007 *Phys. Rev. Lett.* **99** 235503
[14] Damasceno P F, Glotzer S C and Engel M 2017 *J. Phys.: Condens. Matter* **29** 234005
[15] Pattabhiraman H and Dijkstra M 2017 *Soft Matter* **13** 4418
[16] Pattabhiraman H and Dijkstra M 2017 *J. Chem. Phys.* **146** 114901
[17] Pattabhiraman H and Dijkstra M 2017 *J. Phys.: Condens. Matter* **29** 094003
[18] Franzese G 2007 *J. Mol. Liq.* **136** 267
[19] Malescio G, Franzese G, Pellicane G, Skibinsky A, Buldyrev S V and Stanley H E 2002 *J. Phys.: Condens. Matter* **14** 2193
[20] Malescio G and Pellicane G 2004 *Phys. Rev.* E **70** 021202
[21] Skibinsky A, Buldyrev S V, Franzese G, Malescio G and Stanley H E 2004 *Phys. Rev.* E **69** 061206
[22] Malescio G 2007 *J. Phys.: Condens. Matter* **19** 073101
[23] Yan Z, Buldyrev S V, Giovambattista N, Debenedetti P G and Stanley H E 2006 *Phys. Rev.* E **73** 051204
[24] de Oliveira A B, Franzese G, Netz P A and Barbosa M C 2008 *J. Chem. Phys.* **128** 064901
[25] de Oliveira A B, Netz P A, Colla T and Barbosa M C 2006 *J. Chem. Phys.* **125** 124503
[26] Fomin Y D, Gribova N V, Ryzhov V N, Stishov S M and Frenkel D 2008 *J. Chem. Phys.* **129** 064512
[27] Kryuchkov N P, Yurchenko S O, Fomin Y D, Tsiok E N and Ryzhov V N 2018 *Soft Matter* **14** 2152
[28] Gabriëlse A, Löwen H and Smallenburg F 2017 *Materials* **10** 1280
[29] Fornleitner J and Kahl G 2008 *Europhys. Lett.* **82** 18001
[30] Fornleitner J and Kahl G 2010 *J. Phys.: Condens. Matter* **22** 104118
[31] Singh M, Liu H, Kumar S K, Ganguly A and Chakravarty C 2010 *J. Chem. Phys.* **132** 074503
[32] Fomin Y D, Tsiok E N and Ryzhov V N 2019 *Phys. Stat. Mech. Appl.* **527** 121401
[33] Dotera T, Oshiro T and Ziherl P 2014 *Nature* **506** 208–11
[34] Gaiduk E A, Fomin Y D, Tsiok E N and Ryzhov V N 2019 *Mol. Phys.* **117** 2910–19
[35] Kumar A and Molinero V 2017 *J. Phys. Chem. Lett.* **8** 5053
[36] Pérez-Lemus G R, Armas-Pérez J C, Mendoza A, Quintana-H J and Ramírez-Hernández A 2019 *J. Phys.: Condens. Matter* **31** 475102
[37] Marechal M, Zimmermann U and Lowen H 2012 *J. Chem. Phys.* **136** 144506
[38] Berezinskii V L 1971 *Sov. Phys. JETP* **32** 493
[39] Kosterlitz M and Thouless D J 1973 *J. Phys. C Solid State Phys.* **6** 1181
[40] Halperin B I and Nelson D R 1978 *Phys. Rev. Lett.* **41** 121
[41] Nelson D R and Halperin B I 1979 *Phys. Rev.* B **19** 2457
[42] Young A P 1979 *Phys. Rev.* B **19** 1855
[43] Bernard E P and Krauth W 2011 *Phys. Rev. Lett.* **107** 155704
[44] Engel M, Anderson J A, Glotzer S C, Isobe M, Bernard E P and Krauth W 2013 *Phys. Rev.* E **87** 042134
[45] Qi W, Gantapara A P and Dijkstra M 2014 *Soft Matter* **10** 5449
[46] Kapfer S C and Krauth W 2015 *Phys. Rev. Lett.* **114** 035702
[47] Thorneywork A L, Abbott J L, Aarts D G A L and Dullens R P A 2017 *Phys. Rev. Lett.* **118** 158001
[48] Nosé S 1984 *J. Chem. Phys.* **81** 511
[49] Hoover W G 1985 *Phys. Rev.* A **31** 1695
[50] Anderson J A, Lorenz C D and Travesset A 2008 *J. Comput. Phys.* **227** 5342–59
[51] Glaser J, Nguyen T D, Anderson J A, Liu P, Spiga F, Millan J A, Morse D C and Glotzer S C 2015 *Comput. Phys. Commun.* **192** 97–107
[52] de Berg M, van Kreveld M, Overmars M and Schwarzkopf O 2000 *Computational Geometry: Algorithms and Applications* (Berlin: Springer) (Doi: 10.5555/1370949)
[53] McBride C and Wilson M R 1999 *Mol. Phys.* **97** 511–22
[54] Mulero A, Cachadiña I and Solana J R 2009 *Mol. Phys.* **107** 14
[55] Prestipino S, Saija F and Giaquinta P V 2011 *Phys. Rev. Lett.* **106** 235701
[56] Prestipino S, Saija F and Giaquinta P V 2012 *J. Chem. Phys.* **137** 104503
[57] Dudalov D E, Fomin Y D, Tsiok E N and Ryzhov V N 2014 *Soft Matter* **10** 4966
[58] Furlan A P, Lomba E and Barbosa M C 2017 *J. Chem. Phys.* **146** 144503
[59] Engel M, Anderson J A, Glotzer S C, Isobe M, Bernard E P and Krauth W 2013 *Phys. Rev.* E **87** 042134
[60] Stukowski A 2010 *Model. Simulat. Mater. Sci. Eng.* **18** 015012
[61] Schoberth H G, Emmerich H, Holzinger M, Dulle M, Foster S and Gruhn T 2016 *Soft Matter* **12** 7644
[62] Archer A J, Rucklidge A M and Knobloch E 2013 *Phys. Rev. Lett.* **111** 165501
[63] Pattabhiraman H, Gantapara A P and Dijkstra M 2015 *J. Chem. Phys.* **143** 164905